STEEL FIBER REINFORCED SELF-COMPACTING CONCRETE – FROM THE MATERIAL CHARACTERIZATION TO THE STRUCTURAL ANALYSIS

Author: Joaquim A. O. Barros, ISISE, Dep. Civil Eng., University of Minho, barros@civil.uminho.pt

Abstract

Steel fiber reinforced self-compacting concrete (SFRSCC) is a relatively recent material that combines the benefits of a self-consolidated material with those derived from adding fibers to a cement based material, resulting a composite material that can be used in several structural applications with technical and economic advantages, when compared to traditional reinforcement solutions. The present paper summarizes the main achievements obtained in research programs carried out at the Department of Civil Engineering of Minho University, within the ambit of SFRSCC technology. The covered topics are: mix design; fiber pullout; age influence on the compression and flexural behavior; modeling the monotonic and cyclic compression behavior; flexural and punching resistance of prototypes and full scale panels; material nonlinear analysis under the framework of FEM.

1 – INTRODUCTION

Steel Fiber Reinforced Self-Compacting Concrete (SFRSCC) can be defined as a steel fiber reinforced concrete that is able to flow in the interior of the formwork, filling it in a natural manner. SFRSCC has also the capability of passing through the obstacles, flowing and consolidating under the action of its own weight. Due to the relatively high content of fine particles applied to the manufacture of SFRSCC, a stiff and strong fiber-matrix interface can be achieved, which is a favorable medium to mobilize the fiber reinforcement mechanisms, resulting in a material of high post-cracking resistance and ductility, provided that the fiber rupture is avoided. The high compacity of this material and the ability of the fiber reinforcement system to assure diffuse micro-crack patterns can contribute to the development of more durable concrete materials. However, the addition of steel fibers to granular cement based materials perturbs the flowing ability of fresh concrete, which requires special mix methodologies to assure SCC characteristics (Gomes 2002, Pereira 2006).

SFRSCC is especially appropriate for the precast industry, since a high quality control on the materials constituents can be assured, as well as on the mixing, casting and curing procedures. Due to the inherent reinforcement provided by fiber addition, several structural elements, especially those having difficulties in assuring good casting conditions when using conventional concrete, can be manufactured with SFRSCC with technical, economic and aesthetics benefits. However, to enlarge the number, type and relevance of structural applications in SFRSCC, even in precast industry, much more research is needed covering the aspects related to: mechanical properties of the material; design on the perspective of structural stability and durability; development of more sophisticated numerical tools able to simulate the behavior of complex SFRSCC structures up to their failure. The present work has the purpose of contributing to this aim.

2 – MIX DESIGN AND SFRSCC COMPOSITIONS

In general, the materials used for the development of SFRSCC, within the scope of the experimental programs of the present work, were cement (C) CEM I 42.5R (rapid hardening and high strength cement, according to EN197-1:2000), limestone filler (LF), a third generation superplasticizer (SP) based on polycarboxilates (Glenium® 77 SCC), water (W), three types of aggregates (fine river sand (FS), coarse river sand (CS) and crushed granite 5-12 mm (CG)) and DRAMIX® RC-80/60-BN hooked end steel fibers. This fiber has a length (l_f) of 60 mm, a diameter (d_f) of 0.75 mm, an aspect ratio (l_f/d_f) of 80 and a yield stress of 1100 MPa. The methodology followed to formulate SFRSCC compositions is mainly based on the three following steps: i) the proportions of the constituent materials of the binder paste are defined; ii) the proportions of each aggregate on the final granular skeleton are determined; iii) binder paste and granular skeleton are mixed in distinct proportions until self-compacting requirements in terms of spread ability, correct flow velocity, filling ability, blockage and segregation resistance are met, allowing the determination of the optimum paste content in concrete. A detailed description of the method can be found elsewhere (Pereira 2006). Table 2.1 includes the developed SFRSCC compositions (the amount of water referred does not include the aggregate's saturation water). The first composition was used to assess the influence of the age on both the compressive strength and Young's Modulus of the SFRSCC. This SFRSCC was also used to evaluate the punching and the flexural resistance of panel prototypes. The second composition was used in the fiber pullout tests to determine the influence of fiber embedment length, fiber orientation and fiber

anchorage characteristics on the fiber force-slip relationship. This and the third compositions were used in an experimental program dedicated to the evaluation of analytical expressions able to simulate the compression behavior, according to the format of CEB-FIP Model code (1993). The fourth composition was used to appraise the performance of a cyclic analytical model for the simulation of the SFRSCC compression behavior when subjected to cyclic compressive loading. In all compositions the total spread, *s*, was measured, while in the 1st and 4th compositions the time to reach a spread diameter of 500 mm, T_{50}, was also determined (EFNARC 2002). In the 4th composition the H_2/H_1 parameter of the L Box test was also measured (EFNARC 2002). For the developed compositions, no visual sign of segregation was detected and the mixtures showed good homogeneity and cohesion, even while flowing trough the smaller orifice of the Abrams cone (while testing, the Abrams cone was always used in the inverted position).

Table 2.1. SFRSCC compositions per m^3 of concrete

Comp. nº	*C* [kg/m³]	*LF* [kg/m³]	*W* [kg/m³]	*SP* [kg/m³]	*FS* [kg/m³]	*CS* [kg/m³]	*CG* [kg/m³]	*Fibers* [kg/m³]	*SCC requirements*		
									s (mm)	*T_{50} (sec)*	*H2/H1*
1	359.4	308.1	97.0	7.1	172.2	859.2	698.4	30	720	3.5	-
2	359.4	312.2	96.9	6.9	108.2	709.4	665.2	30	700	-	-
3	401.7	344.3	108.4	7.6	101.7	666.4	624.8	45	700	-	-
4	401.7	344.3	117.3	7.7	178.3	668.1	600.0	45	730	7	0.89

3 – FIBER PULLOUT

3.1 – Introduction

The effectiveness of a given fiber as a medium of crack-opening arrestment for cement based materials is often assessed using a single fiber pullout test, where fiber slip is monitored as a function of the applied load on the fiber (Naaman and Najm 1991; Banthia and Trottier 1994; Li and Chan 1994; Groth 2000). The present section focuses on relevant results of a research project dedicated to the evaluation of the pullout behavior of the hooked ends steel fibers indicated in Section 2, when embedded into a SCC medium. The details can be consulted in Cunha *et al.* (2007a).

3.2 – Test series and properties of the intervening materials

The pullout tests of the experimental program can be divided in two main groups, according to the type of used fibers: hooked-ends and smooth. The influence of the various mechanisms of bond can, therefore, be assessed separately. Within these two main groups, the influence of the fiber embedded length and fiber orientation on the fiber pullout response was assessed. Smooth fibers were obtained cutting, with a plier, the hooked ends of RC-80/60-BN fibers. Code names for the series of tests consist of alphanumeric characters separated by underscore. The first character indicates the fiber type (S - smooth; H - hooked), the second string indicates the embedded length in mm (for instance, lb10 represents a fiber embedded length of 10 mm) and finally the last numeral indicates the fiber inclination angle, in degrees, with the fiber pullout load orientation. The complete overview of all the performed fiber pullout tests, with reference to the type, aspect ratio, embedded length (lb) and inclination angle of the fiber, is given in Table 3.1. The 2nd SCC composition of Table 2.1 was used in this experimental program. The concrete compressive strength was assessed by three cubic specimens with an edge length of 150 mm. The average value of the concrete compressive strength, at the age of the fiber pullout tests, was 83.4 MPa with a coefficient of variation of 0.9 %. Moreover, six single fibers were tested under direct tension in order to assess the fiber tensile strength, having resulted a fiber tensile strength of 1141 MPa with a coefficient of variation of 2.0 %. A detailed description of the fiber pullout specimens can be found elsewhere (Cunha *et al.* 2007a).

3.3 – Test setup

The pullout tests were performed in a servo-hydraulic Lloyd LR30K machine with a capacity of 30 kN. To record force values with high accuracy, a HBM S9 load cell with a capacity of 5 kN, and accuracy class 0.05 was attached to the machine test frame. The single-sided specimen was mounted in a steel specimen supporting system, see Figs. 3.1a and 3.1b. This frame incorporates a steel system composed by a plate monolithically connected to a cylinder that is fixed to the testing machine frame. The cylinder/machine connection allows free rotations of the entire steel frame. A steel ring is coupled to the aforementioned steel system by three steel screws. The protruding end of the steel fiber is fastened to a standard “Lloyd" grip, which allows a secure hold of the fiber. However, due to the small fiber diameter, special attention was given in fastening the fiber, since deforming the fiber end could induce that the fiber would break at the grip. For the measurement of the fiber pullout slip, three LVDT's (linear stroke +/- 5mm) were used. To exclude

measuring deformations of the testing rig and fiber slip at the grip, the LVDT's were fixed at the upper steel ring and touching the bottom surface of an aluminum plate fixed to the fiber. The plate was fixed to the fiber with two fine screws and was used as a support for this LVDT configuration (detail in Figs. 3.1(c) and 3.1(d)).

Table 3.1 - Overview of the performed pullout tests.

Series	Fiber type	lb[mm]	Angle [°]	N. specimens
S_lb10_0	Smooth	10	0	-
S_lb10_30			30	-
S_lb10_60			60	3
S_lb20_0		20	0	3
S_lb20_30			30	3
S_lb20_60			60	3
S_lb30_0		30	0	3
S_lb30_30			30	3
S_lb30_60			60	3
H_lb10_0	Hooked	10	0	6
H_lb10_30			30	6
H_lb10_60			60	6
H_lb20_0		20	0	6
H_lb20_30			30	6
H_lb20_60			60	6
H_lb30_0		30	0	6
H_lb30_30			30	6
H_lb30_60			60	6

(a)

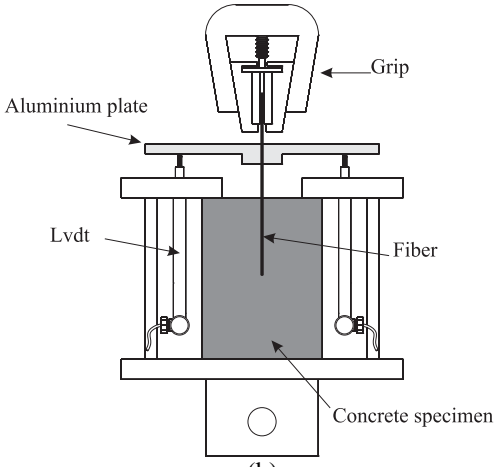

(b)

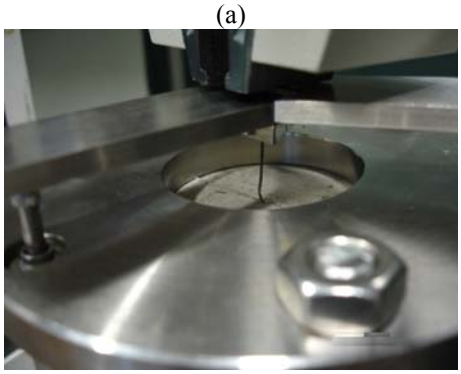

(c)

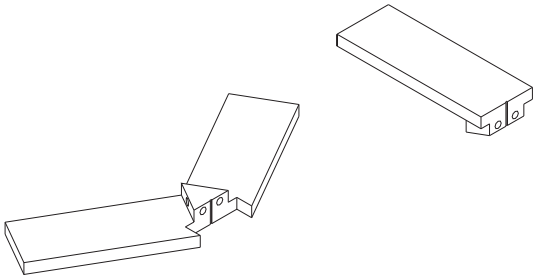

(d)

Fig. 3.1 - Configuration of the single fiber pullout test: (a), (b) general view, and (c), (d) detailed view of the aluminum plate fixed to the fiber.

Since the three LVDT's were disposed around test specimen forming an angle of 120 degrees between consecutive LVDT's, the actual pullout slip of the fiber is the average of the three LVDT's readouts. The

closed-loop displacement control was performed by the testing machine internal displacement transducer, at the displacement rate of 10 μm⁄s.

3.3 – Relevant results

The average pullout load-slip curves for the tested series are depicted in Fig. 3.2. In general, for both analyzed hooked and smooth aligned fibers, the configuration of the pullout load-slip curve was similar, regardless the fiber embedded length but, as expected, the peak load and the dissipated energy increased with it (see Figs. 3.2a and 3.2b). The vertical offset distance between curves can be regarded as the contribution of the embedded bond length increment or decrement between curves. In the case of hooked fibers with a 30º inclination angle, two failure modes occurred, resulting two distinct types of pullout-slip curves. In Fig. 3.2c, the average curve is represented up to the slip where the fiber rupture took place, therefore the curve averaging was performed only up to a slip correspondent to the peak load.

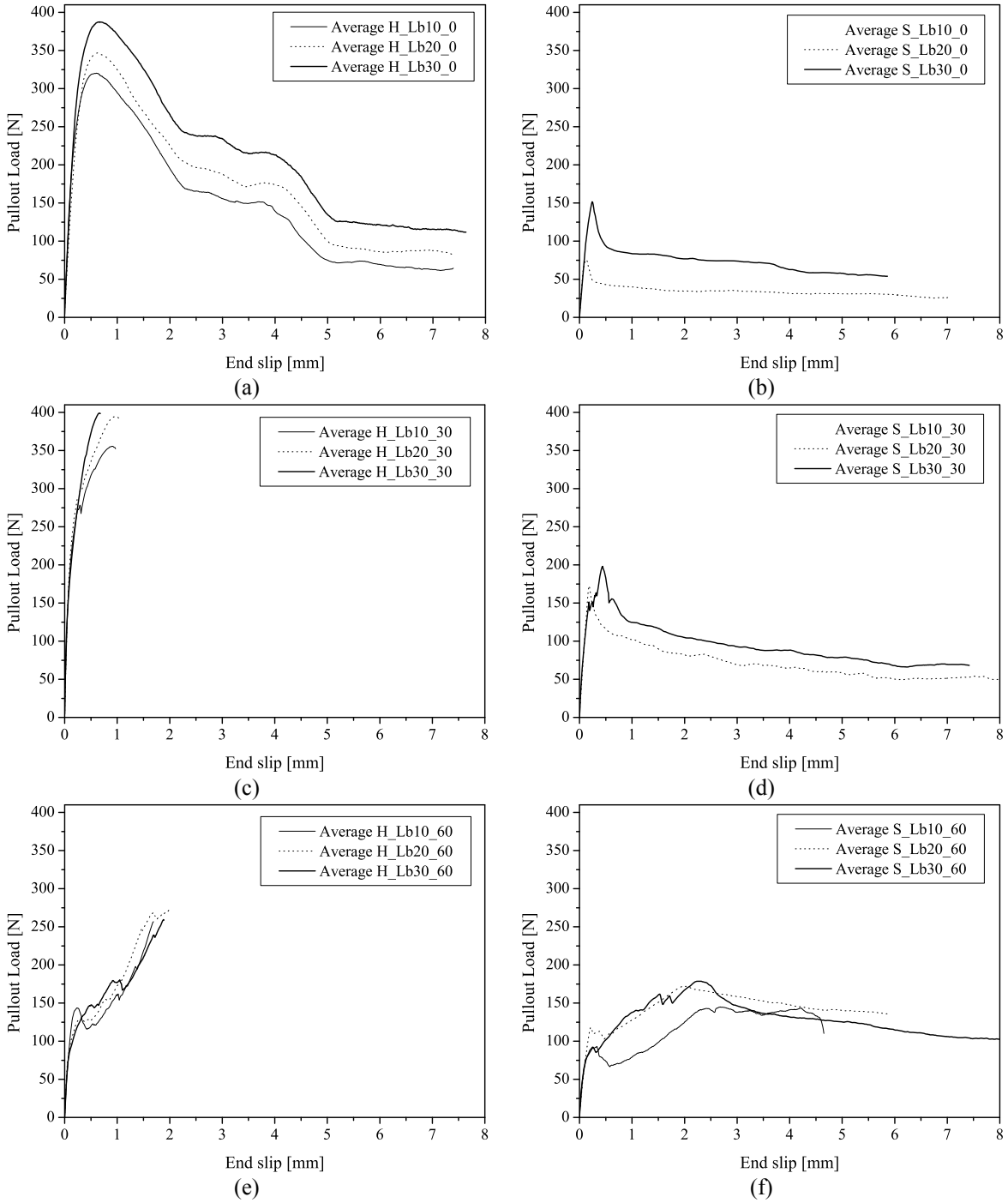

Fig. 3.2 - Average pullout load-slip curves for a fiber inclination angle: (a), (b) 0 degrees; (c), (d) 30 degrees, and (d),(f) 60 degrees.

The pre-peak branch of these curves is similar to the one observed for aligned hooked fibers. The nonlinear part is, however, more pronounced than for aligned fibers, due to the cracking and spalling of the matrix at the fiber bending point, as a consequence of the additional stress concentration at this zone for inclined fibers. Whenever for a 30º inclination angle the hooked fiber did not break, and therefore the fiber was fully pulled out, the post-peak behavior was assessed. The post-peak curve of the latter specimens was similar to the observed for aligned series, however, an increment of the residual force was perceived up to a slip of 4 mm. Such difference is ascribed to the frictional resistance increase due to the force component perpendicular to the fiber axis. Afterwards, at slip of about 4.5 mm (corresponding approximately to the straightened hook length), a significant load decay was observed.

On the other hand, smooth fibers with an inclination angle of 30º revealed two distinct pre-peak behaviors. Regarding the series with an embedded length of 20 mm, the pre-peak behavior was identical to the one observed for the aligned smooth fibers, with the exception that a higher peak load was attained, as a consequence of the bending mechanism associated to fiber inclination angle. For a larger embedded length (30 mm), before reaching the peak load it is observed a decline on the stiffness, subordinated to several load decays corresponding to the cracking or spalling of the concrete matrix (see Fig. 3.2d). With respect to the post-peak behavior, the load decreases with the increase of slip. Comparatively to the aligned smooth fibers, the load decay is lesser abrupt, since the influence of the frictional resistance is more significant for inclined fibers.

A completely distinct behavior was observed for the series with an inclination angle of 60º (Figs. 3.2e and 3f). The hooked series with the latter inclination angle failed by fiber rupture, with the exception of one specimen, whereas in the smooth series, fibers were fully pulled out. As the inclination angle increases, the stresses concentration at the fiber exit point from the matrix increases, therefore the concrete matrix will be more prone to cracking and spalling. In terms of pre-peak behavior, this is reflected in a significant loss of stiffness. Comparing, respectively, Figs. 3.2c, 3.2d, and Figs. 3.2e, 3.2f, can be perceived that for the series with a 60º angle, cracking and spalling starts for a lower load level. Moreover, as a larger portion of concrete is pushed or pulled out, a larger fiber length can be more easily bent, which promotes the stiffness decrease up to the peak load. Regarding the post-peak in smooth fibers a gradual load decay was observed in opposite to both smooth fibers aligned and with a 30º angle, since for a 60º inclination angle the frictional resistance due to the force component perpendicular to the fiber axis is much higher.

4 – CHARACTERIZATION OF THE MECHANICAL PROPERTIES

4.1 - Introduction

This chapter is dedicated to the evaluation of the compression and flexural behavior of the developed SFRSCC. Special attention is given to the evaluation of the age affect on the properties that characterize the SFRSCC compression and flexural behavior.

4.2 – Compression behavior

4.2.1 – Age influence

Scarce research is available on the evaluation and modeling the influence of the SFRSCC age in its compression behavior. A good knowledge of the stress-strain relationship at early ages plays an important role in the determination of the time for the removal of shoring. This is a main concern in the precast industry, since demolding the elements as soon as possible is an important requirement in terms of production profitability. To assure safe demolding process, the influence of the SFRSCC age on its compression behavior should be known. For this purpose, uniaxial compression tests were carried out. The details of the test setup and test procedures are described elsewhere (Cunha *et al.* 2007b). The compositions nº 2 and 3, indicated in Table 2.1, were used in this experimental program, having received the designation of *Cf30* and *Cf45*, the first one reinforced with 30 kg/m^3 of fibers, while the second one with 45 kg/m^3. Stress-strain laws are proposed to model the behavior of the SFRSCC since the early ages. Additionally, expressions derived from fitting the experimental obtained results are proposed to predict the principal mechanical properties of SFRSCC in uniaxial compression.

4.2.1.1 – Material properties

The average stress-strain curves, $\sigma_c - \varepsilon_c$, for the *Cf30* and *Cf45* series are represented in Figs. 4.1a and 4.1b, respectively. Table 4.1 includes the average values of the compressive strength, f_{cm}, and the correspondent coefficients of variation, CoV. As expected, for both series, the f_{cm} increased with the age. Up to 24 hours the compressive strength of *Cf45* was higher than that of *Cf30*. However, after this age the f_{cm} of *Cf30* had a strengthening much more pronounced with time than the one measured in *Cf45*. The justification for this behavior can be found elsewhere (Cunha *et al.* 2007b).

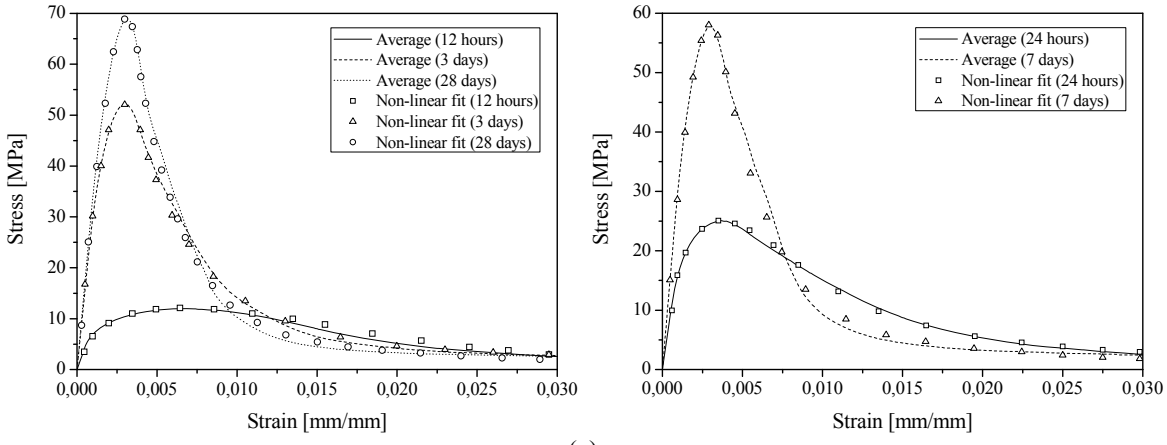

(a)

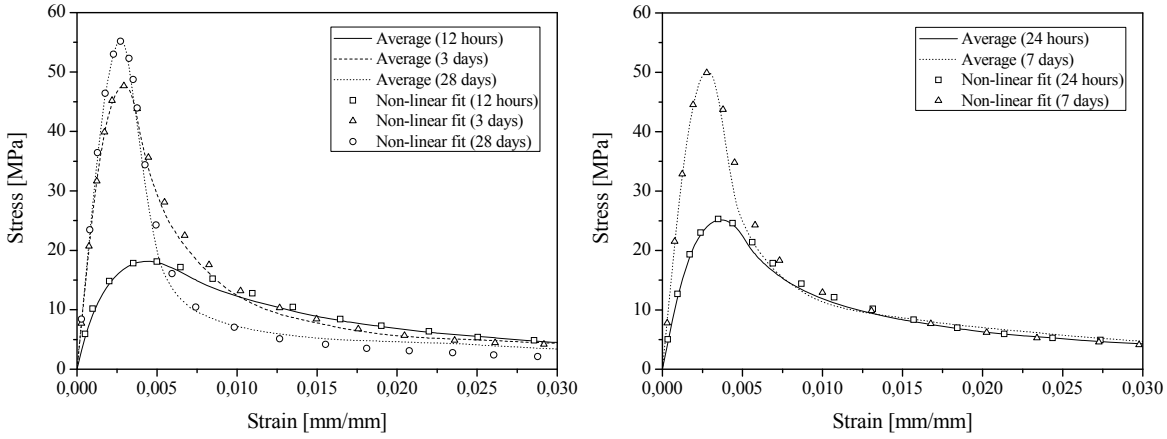

(b)

Fig. 4.1 – Experimental and analytical relationships for: (a) *Cf30* series; (b) *Cf45* series.

The average values of the elasticity modulus, E_{ci}, and the correspondent CoV are also indicated in Table 4.1. The E_{ci} increased with age for both series and had a similar variation with age as f_{cm}. However, for *Cf30* the f_{cm} value increased significantly between 7 and 28 days, while the E_{ci} of *Cf30* had a marginal increment in this period. After the age of three days, the E_{ci} of *Cf45* had an increment of only 3 GPa. These results point out that the stiffness of both SFRSCC is at the age of 3 days approximately 90% of the stiffness at 28 days, due to the high matrix compacity of these concretes. The difference between the values of elasticity modulus of *Cf30* and *Cf45* series may be due to the influence of the curing temperature and content of limestone filler, as is justified elsewhere (Cunha *et al.* 2007b). The influence of SFRSCC age on its toughness was also evaluated (Cunha *et al.* 2007b).

Table 4.1 – Average values of the compressive strength and elasticity modulus.

Age	***Cf30***				***Cf45***			
	f_{cm} [MPa]	CoV [%]	Eci [GPa]	CoV [%]	f_{cm} [MPa]	CoV [%]	Eci [GPa]	CoV [%]
12 hours	12.3	9.95	13.6	17.86	17.6	1.63	18.8	7.10
24 hours	24.7	8.38	25.3	4.96	25.3	1.24	22.4	5.83
3 days	52.3	1.90	37.1	4.31	47.9	1.10	31.4	2.04
7 days	58.1	4.32	40.4	0.78	51.0	2.61	31.9	2.14
28 days	69.7	1.73	41.5	2.31	56.2	2.15	34.5	4.33

4.2.1.2 – Modeling the compression behavior according to the EC2 format

To estimate the compressive strength and the Young's Modulus of plain concrete (PC) at various ages, $f_{cm}(t)$ and $E_{ci}(t)$, respectively, the CEB-FIP Model code (MC90 1993) suggests the followings Eqs.:

$$f_{cm}(t) = f_{cm}(28) \cdot \exp\left\{a\left[1-\left(\frac{28}{t}\right)^{b}\right]\right\} \tag{4.1}$$

$$E_{ci}(t) = E_{ci}(28) \cdot \left\{ \exp\left[a\left(1 - \left(\frac{28}{t} \right)^{b} \right) \right] \right\}^{c} \tag{4.2}$$

$$E_{ci} = E_{c0} \cdot \left(\frac{f_{cm}}{f_{cm0}} \right)^{a} \tag{4.3}$$

where $f_{cm}(28)$ and $E_{ci}(28)$ are the average compressive strength and Young's modulus at 28 days, respectively, and values for a, b, c, E_{c0} and f_{cm0} were proposed by the MC90 for PC. For the developed SFRSCC new values for these parameters, indicated in Figs. 4.2 to 4.4, were obtained applying the non-linear fitting method (Cunha *et al.* 2006).

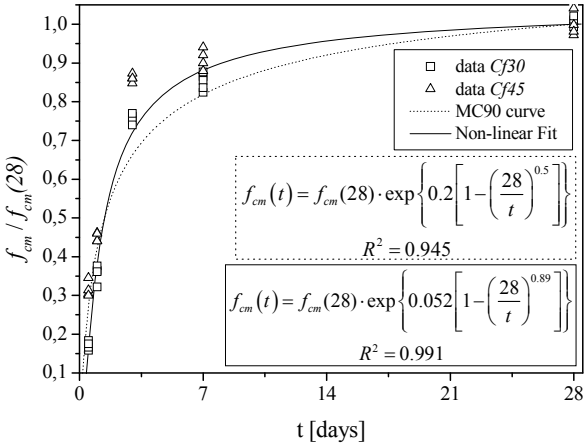

Fig. 4.2 – Simulation of the age influence on the concrete compressive strength.

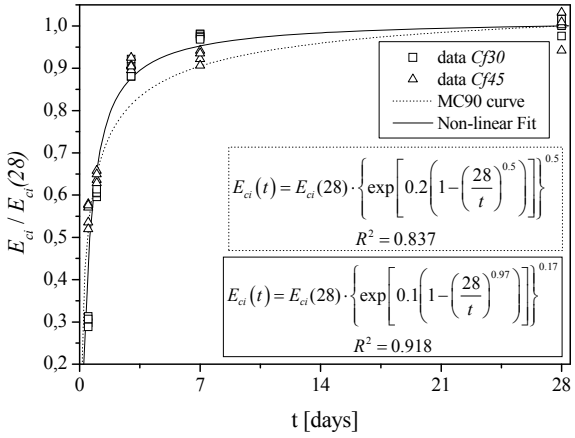

Fig. 4.3 – Simulation of the age influence on the concrete elasticity modulus.

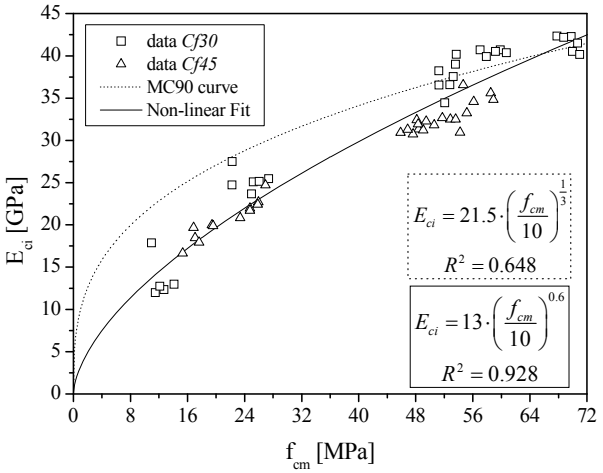

Fig. 4.4 – Relationship between the concrete elasticity modulus and the compressive strength.

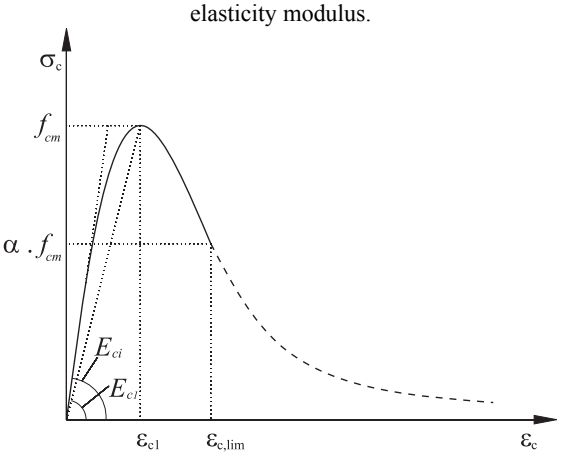

Fig. 4.5 – Stress-strain diagram for uniaxial compression.

To simulate the stress-strain behavior of the developed SFRSCC it was used the Eq. proposed by the MC90 for PC, which is schematically represented in Fig. 4.5. The branch represented by a full line is simulated by the following function:

$$\sigma_c(\varepsilon_c) = \frac{\dfrac{E_{ci}}{E_{c1}} \cdot \dfrac{\varepsilon_c}{\varepsilon_{c1}} - \left(\dfrac{\varepsilon_c}{\varepsilon_{c1}} \right)^2}{1 + \left(\dfrac{E_{ci}}{E_{c1}} - 2 \right) \cdot \dfrac{\varepsilon_c}{\varepsilon_{c1}}} \cdot f_{cm} \quad \text{for} \quad \varepsilon_c \le \varepsilon_{c,\lim} \tag{4.4}$$

where E_{ci} and E_{c1} are, respectively, the tangent modulus and the secant modulus from the origin to the compressive strength, $E_{c1} = f_{cm} / \varepsilon_{c1}$; σ_c, ε_c and ε_{c1} are the compressive stress, the compressive strain and

the strain at the compressive strength, respectively. The strain $\varepsilon_{c,\lim}$ limits the applicability of Eq. (4.4), see Fig. 4.5. For the descending part of the stress-strain diagram, Eq. 4.4 is valid only for strain values up to $\varepsilon_{c,\lim}$. The strain $\varepsilon_{c,\lim}$ at $\sigma_{c,\lim}$ $\left(=\alpha \cdot f_{cm}\right)$ is computed from the following Eq. (Cunha *et al.* 2006):

$$\varepsilon_{c,\lim} = \left[\frac{1}{2}\left[\left(1-\alpha\right)\cdot\frac{E_{ci}}{E_{c1}}+2\alpha\right]+\left[\frac{1}{4}\left[\left(1-\alpha\right).\frac{E_{ci}}{E_{c1}}+2\alpha\right]^2-\alpha\right]^{0.5}\right]\varepsilon_{c1} \tag{4.5}$$

For $\varepsilon_c > \varepsilon_{c,\lim}$ the descending branch of the $\sigma_c - \varepsilon_c$ diagram (dashed line in Fig. 4.5) is defined using an Eq. of the type:

$$\sigma\left(\varepsilon_c\right) = \left[a\left(\frac{\varepsilon_c}{\varepsilon_{c1}}\right)^2 + b\frac{\varepsilon_c}{\varepsilon_{c1}}\right]^{-1}\cdot f_{cm} \quad \text{for} \quad \varepsilon_c > \varepsilon_{c,\lim} \tag{4.6}$$

where the values of parameters a and b are determined in order to assure the continuity of the function at the point $\varepsilon_c = \varepsilon_{c,\lim}$. Since the following conditions should be assured:

$$\underbrace{\sigma_c\left(\varepsilon_{c,\lim}\right)}_{\text{equation (4.4)}} = \underbrace{\sigma_c\left(\varepsilon_{c,\lim}\right)}_{\text{equation (4.6)}} \quad \wedge \quad \underbrace{\left.\frac{\partial\sigma_c}{\partial\varepsilon_c}\right|_{\varepsilon_{c,\lim}}}_{\text{equation (4.4)}} = \underbrace{\left.\frac{\partial\sigma_c}{\partial\varepsilon_c}\right|_{\varepsilon_{c,\lim}}}_{\text{equation (4.6)}} \tag{4.7}$$

Eq. (4.6) is converted into the following one:

$$\sigma\left(\varepsilon_c\right) = \left[\left[\frac{1}{\frac{\varepsilon_{c,\lim}}{\varepsilon_{c1}}}\xi\cdot\left(\frac{1}{2\alpha}\right)^2 - \frac{1}{\left(\frac{\varepsilon_{c,\lim}}{\varepsilon_{c1}}\right)^2}\cdot\frac{1}{\alpha}\right]\left(\frac{\varepsilon_c}{\varepsilon_{c1}}\right)^2 + \left[\frac{1}{\frac{\varepsilon_{c,\lim}}{\varepsilon_{c1}}}\cdot\frac{2}{\alpha} - \xi\left(\frac{1}{2\alpha}\right)^2\right]\frac{\varepsilon_c}{\varepsilon_{c1}}\right]^{-1}\cdot f_{cm} \tag{4.8}$$

with

$$\xi = \frac{4\left[\left(\frac{\varepsilon_{c,\lim}}{\varepsilon_{c1}}\right)^2\cdot\left(\frac{E_{ci}}{E_{c1}}-2\right)+2\frac{\varepsilon_c}{\varepsilon_{c1}}-\frac{E_{ci}}{E_{c1}}\right]}{\left[\frac{\varepsilon_{c,\lim}}{\varepsilon_{c1}}\left(\frac{E_{ci}}{E_{c1}}-2\right)+1\right]^2} \tag{4.9}$$

The analytical stress-strain curves obtained from the best fit procedure and the experimental average stress-strain curves are depicted in Fig. 4.1. The accuracy of the proposed expression toward the experimental data is quite high. Fig. 4.6 presents an exponential function used to estimate the evolution of the parameter α with the age. The value suggested by MC90 for PC is also represented.

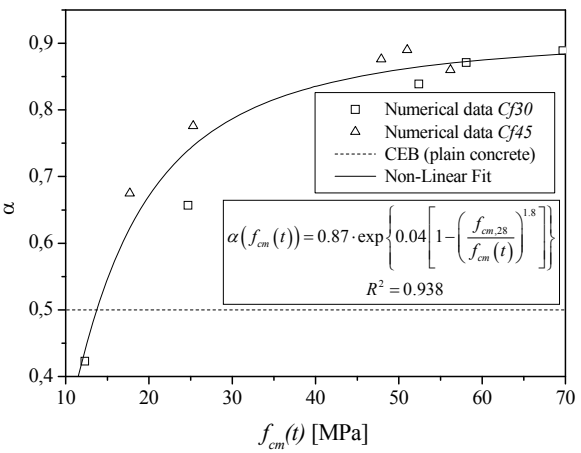

Fig. 4.6 - Relationship between parameter α and compressive strength.

4.2.2 – Cyclic behavior

To evaluate the compression cyclic behavior of SFRSCC, another experimental program was carried out with the specimens molded from the composition nº 4 (Table 2.1). The results derived from this experimental program were used to appraise a constitutive model to simulate the cyclic compression behavior of the developed SFRSCC. This experimental program is composed of nine cylinder specimens (150 mm diameter, 300 mm height), six of them were tested with cyclic compressive loading, while the remaining three specimens were tested with monotonic loading, at the age of 14 days. At this age, the developed SFRSCC presented an average value for the Young's Modulus and compressive strength of 36 GPa and 55 MPa, respectively. Fig. 4.7 shows typical cyclic and monotonic stress-strain curves obtained in this experimental program. It is evident that the monotonic curve corresponds to the envelope of the cyclic curve. All the results can be found elsewhere (Gonçalves and Barros 2007).

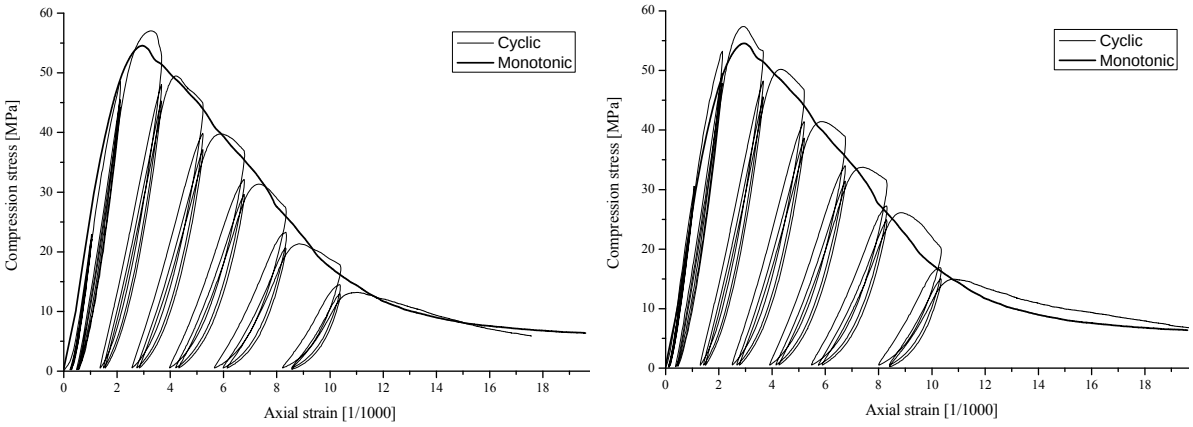

Fig. 4.7 - Typical cyclic versus monotonic stress-strain relationship obtained in experimental program: (a) Cyl9, (b) Cyl10 specimens.

The model adopted to simulate the compression hysteretic behavior of SFRSCC is schematically represented in Fig. 4.8. A general hysteretic scheme is simulated by the paths $\overline{BC}$, $\overline{CD}$, $\overline{DE}$, $\overline{EF}$ and $\overline{FG}$. These paths are simulated by the following Eqs. (negative signal was assumed for compression in this model):

$$\sigma_c = \overline{\sigma}_c^{\min}\left(\frac{\varepsilon_c - \varepsilon_c^{pl}}{\overline{\varepsilon}_c^{\min} - \varepsilon_c^{pl}}\right)^a \quad if \quad \begin{cases} \varepsilon_{cu} < \varepsilon_c^{\min} \le 0 \\ \varepsilon_c^{\min} < \varepsilon_c \le \varepsilon_c^{pl} \quad (\overline{BC} \text{ and } \overline{DE}) \\ \Delta\varepsilon_c > 0 \end{cases} \tag{4.10}$$

$$\sigma_c = \sigma_{c(pf)}^{urc} + \left(\overline{\sigma}_c^{\min} - \sigma_{c(pf)}^{urc}\right)\left(\frac{\varepsilon_c - \varepsilon_{c(pf)}^{urc}}{\overline{\varepsilon}_c^{\min} - \varepsilon_{c(pf)}^{urc}}\right) \quad if \quad \begin{cases} \varepsilon_{cu} < \varepsilon_c^{\min} \le 0 \\ \varepsilon_c^{\min} < \varepsilon_c \le \varepsilon_c^{pl} \quad (\overline{CD} \text{ and } \overline{EF}) \\ \Delta\varepsilon_c \le 0 \end{cases} \tag{4.11}$$

$$\sigma_c = \sigma_{cf}^{rec} + E_{c,env}^{rec}\left(\varepsilon_c - \varepsilon_{cf}^{rec}\right) + b\left(\varepsilon_c - \varepsilon_{cf}^{rec}\right)^2 \quad if \quad \begin{cases} \varepsilon_{cu} < \varepsilon_c^{\min} \le 0 \\ \varepsilon_{cf}^{rec} < \varepsilon_c \le \varepsilon_c^{\min} \quad (\overline{FG}) \\ \Delta\varepsilon_c \le 0 \end{cases} \tag{4.12}$$

The monotonic branches $\overline{OB}$ and $\overline{GH}$ are simulated by the monotonic stress-strain relationship. Eq. (4.10) simulates the paths $\overline{BC}$ and $\overline{DE}$, i.e., both the partial and full unloading branches. In case of $\overline{BC}$ $\overline{\varepsilon}_c^{\min} = \varepsilon_{cons}^{unl}$ is the strain at point B, at the onset of unloading, and $\overline{\sigma}_c^{\min} = \sigma_{cons}^{unl}$ its corresponding stress, while in the case of $\overline{DE}$, $\overline{\varepsilon}_c^{\min} = \varepsilon_{cp}^{ruc}$ and $\overline{\sigma}_c^{\min} = \sigma_{cp}^{ruc}$, which is evaluated from the following equation:

$$\sigma_{cp}^{ruc} = \sigma_{cp}^{urc} + \left(\frac{\sigma_{cf}^{rel} - \sigma_{cp}^{urc}}{\varepsilon_c^{\min} - \varepsilon_{cp}^{urc}} \right) \left(\varepsilon_{cp}^{ruc} - \varepsilon_{cp}^{urc} \right) \tag{4.13}$$

where

$$\sigma_{cf}^{rel} = 0.92\, \sigma_{cons}^{unl} + 0.08\, \sigma_{cp}^{urc} \tag{4.14}$$

which is responsible for modeling the degradation in the compressive reloading stiffness. In Eq. (4.10) ε_c^{pl} is the compressive plastic strain that, according to Okamura and Maekawa (1991) can be evaluated from the following Eq.:

$$\varepsilon_c^{pl} = \varepsilon_c^{\min} - \frac{20}{7} \left[1 - \exp\left(-0.35 \frac{\varepsilon_c^{\min}}{\varepsilon_{c1}} \right) \right] \varepsilon_{c1} \tag{4.15}$$

The *a* shape factor of Eq. (4.10) can be determined from the Eq. proposed by Wang *et al.* (1981):

$$a = 1.0 + 0.7 \left(\frac{\varepsilon_c^{\min}}{\varepsilon_{c1}} \right) \tag{4.16}$$

Eq. (4.11) simulates the paths $\overline{CD}$ and $\overline{EF}$, i.e., the partial reloading and the reloading up to the experienced minimum compressive strain (ε_{cons}^{unl}). For the partial reloading, branch $\overline{CD}$, $\varepsilon_{c(pf)}^{urc} = \varepsilon_{cp}^{urc}$ and $\sigma_{c(pf)}^{urc} = \sigma_{cp}^{urc}$ are the strain and the stress at point C. For this branch, $\overline{\varepsilon}_c^{\min} = \varepsilon_{cons}^{unl}$ and $\overline{\sigma}_c^{\min} = \sigma_{cp}^{ruc}$, where σ_{cp}^{ruc} is calculated from Eqs. (4.13) and (4.14). In the case of the branch $\overline{EF}$, $\varepsilon_{c(pf)}^{urc} = \varepsilon_{cf}^{urc} = \varepsilon_c^{pl}$, $\sigma_{c(pf)}^{urc} = \sigma_{cf}^{urc} = 0$, $\overline{\varepsilon}_c^{\min} = \varepsilon_{cp}^{ruc}$ and $\overline{\sigma}_c^{\min} = \sigma_{cp}^{ruc}$, with σ_{cp}^{ruc} calculated from Eqs. (4.13) and (4.14).
The strain of the returning point G on the compressive envelope curve can be obtained from the following equation:

$$\varepsilon_{cf}^{rec} = \varepsilon_{cons}^{unl} + \frac{4}{3} \left(\frac{\sigma_{cons}^{unl} - \sigma_{cf}^{rel}}{\sigma_{cf}^{rel}} \right) \left(\varepsilon_{cons}^{unl} - \varepsilon_c^{pl} \right) \tag{4.17}$$

and the corresponding stress, σ_{cf}^{rec}, is determined replacing ε_c by ε_{cf}^{rec} on the envelope curve.

Finally, Eq. (4.12) simulates the path $\overline{FG}$, i.e., the returning to the envelop curve, where

$$E_{c,env}^{rec} = \left. \frac{d\sigma_c}{d\varepsilon_c} \right|_{\varepsilon = \varepsilon_{cf}^{rec}}^{env} \tag{4.18}$$

is the tangent to the envelope curve, evaluated at the strain ε_{cf}^{rec}, and *b* factor is determined from:

$$b = \frac{\sigma_{cf}^{rel} - \sigma_{cf}^{rec} - E_{c,env}^{rec} \left(\varepsilon_{cons}^{unl} - \varepsilon_{cf}^{rec} \right)}{\left(\varepsilon_{cons}^{unl} - \varepsilon_{cf}^{rec} \right)^2} \tag{4.19}$$

This model was applied to the simulation of the cyclic compression tests. The comparison is presented in Fig. 4.9, from which it can be concluded that the model simulates with high accuracy the compression cyclic behavior of SFRSCC specimens.

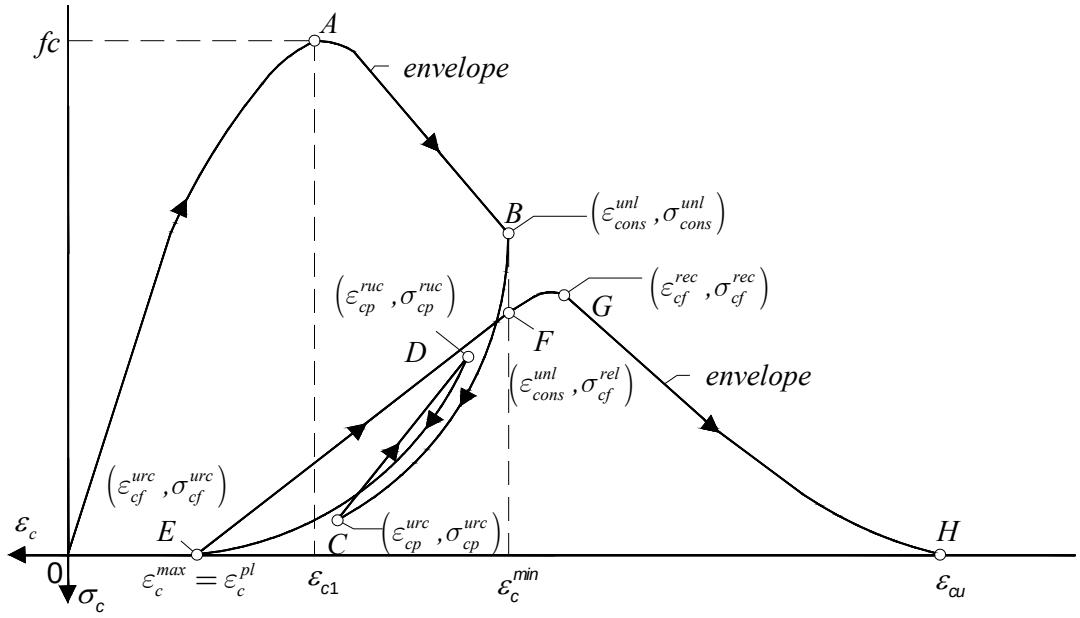

Fig. 4.8 - Cyclic hysteretic model for SFRSCC.

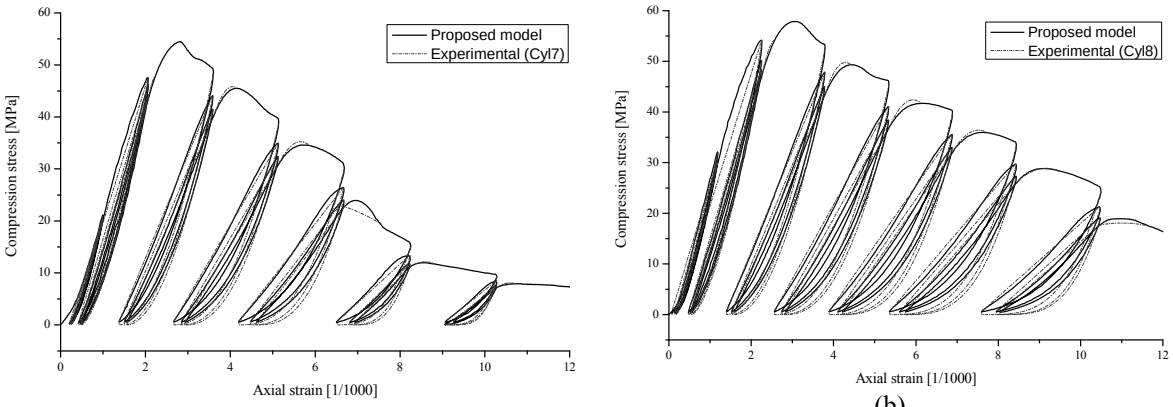

Fig. 4.9 - Experimental and analytical stress-strain curves cyclic compression tests: (a) Cyl7, (b) Cyl8 specimens

4.3 – Flexural behavior

4.3.1 – Test setup and design parameters

The composition nº 1 (Table 2.1) was used to assess the influence of the SFRSCC age on its flexural behavior. In the carried out tests, the recommendations of RILEM TC 162-TDF (Vandewalle *et al.* 2002) were adopted in terms of curing procedures, position and dimensions of the notch sawn into the specimen, load and specimen support conditions, characteristics for both the equipment and measuring devices, and test procedures. The method for casting the beam specimens proposed by RILEM TC 162-TDF was adapted for SFRSCC, since they were cast without any external compaction energy. From the obtained force-deflection relationship, the equivalent ($f_{eq,2}$ and $f_{eq,3}$) and the residual ($f_{R,1}$ and $f_{R,4}$) flexural tensile strength parameters can be evaluated. The parameters $f_{eq,2}$ and $f_{eq,3}$ are related to the material energy absorption capacity up to a deflection of δ_2 and δ_3 ($\delta_2 = \delta_L + 0.65$mm and $\delta_3 = \delta_L + 2.65$mm, where δ_L is the deflection corresponding to the highest load recorded up to a deflection of 0.05 mm) provided by fiber reinforcement mechanisms ($D^f_{BZ,2}$ and $D^f_{BZ,3}$), as seen in Fig. 4.10. The parcel of the energy due to matrix cracking (D^b_{BZ}) is not considered in the f_{eq} evaluation. The parameters $f_{R,1}$ and $f_{R,4}$ are the stresses for the forces $F_{R,1}$ and $F_{R,4}$, respectively, at deflections of $\delta_{R,1}$ = 0.46 mm and $\delta_{R,4}$ = 3.0 mm. According to RILEM TC 162-TDF, the equivalent (Vandewalle *et al.* 2000) and the residual (Vandewalle *et al.* 2002) flexural tensile strength parameters are obtained from the following Eqs.:

$$f_{eq,2} = \frac{3}{2}\frac{D^f_{BZ,2}}{0.50}\frac{L}{bh^2_{sp}}\ ;\ f_{eq,3} = \frac{3}{2}\frac{D^f_{BZ,3}}{2.50}\frac{L}{bh^2_{sp}}\ \text{[N/mm}^2\text{]} \tag{4.20}$$

$$f_{R,1} = \frac{3}{2}\frac{F_{R,1}L}{bh^2_{sp}}\ ;\ f_{R,4} = \frac{3}{2}\frac{F_{R,4}L}{bh^2_{sp}}\ \text{[N/mm}^2\text{]} \tag{4.21}$$

where b (=150 mm) and L (=500 mm) are the width and the span of the specimen, and h_{sp} (=125 mm) is the distance between the tip of the notch and the top of the cross section.

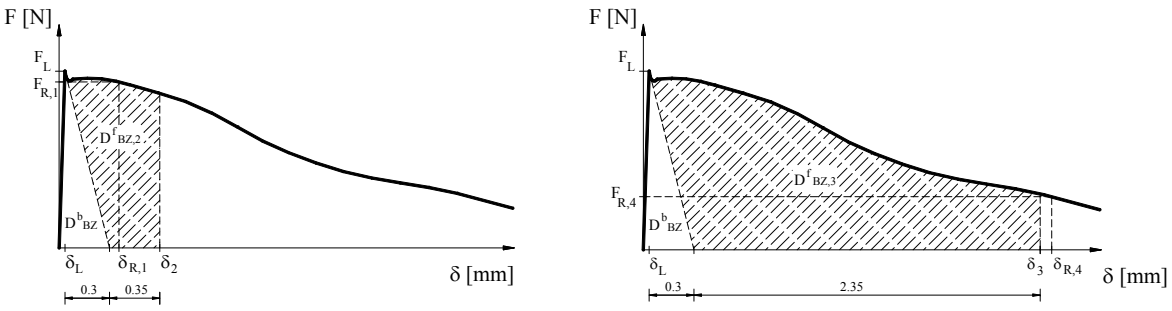

(a) (b)

Fig. 4.10 - Evaluation of (a) $f_{eq,2}$ and $f_{R,1}$, and (b) $f_{eq,3}$ and $f_{R,4}$ flexural tensile strength parameters according to RILEM TC 162-TDF (Adapted from Vandewalle *et al.* 2000, 2002).

4.3.2 – Relevant results

The force-deflection curves, F-δ, obtained in the tested series are depicted in Fig. 4.11. Each curve represents the average of the F-δ relationship values recorded in three specimens. This figure shows that, just after the deflection δ_L, a load decay occurred with an amplitude that also increased with the SFRSCC age, since a higher load had to be sustained by the fibers bridging the specimen fracture surface. This load decay was followed by a hardening phase up to a deflection level that decreased with the SFRSCC age. With the exception of the 12 hours series, all series exhibited a post-crack hardening phase followed by a softening branch. The decrease of residual strength in the softening branch was much more pronounced in series of specimens of 28 days. The larger amplitude of load decay, just after δ_L, observed in 28 days series would have adversely affected the fiber-concrete bond properties and the fiber anchorage effectiveness, leading to a decrease in the force necessary to pullout the fibers bridging the specimen's fracture surface. This fact may be the reason the equivalent (f_{eq}) and residual (f_R) flexural tensile strength parameters were lower at 28 days as compared to 7 days, as shown in Fig. 4.12. This decrease was more pronounced in $f_{R,4}$ curve, since this parameter is directly dependent on the shape of the force-deflection curve, and is evaluated for the largest measured deflection. As $f_{eq,2}$ and $f_{R,1}$ had similar variation with the age, it may be concluded that, for low values of deflection (δ_2 and $\delta_{R,1}$), the energy and the force based concepts provide identical results in this case.

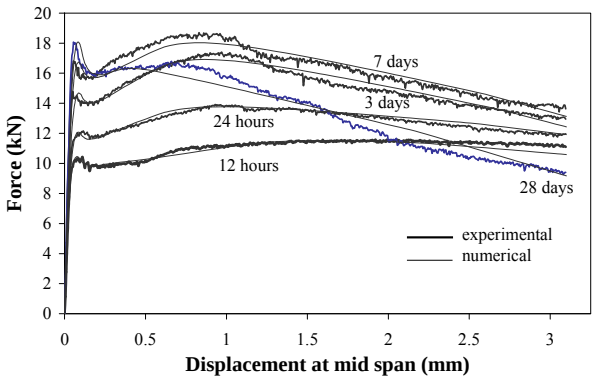

Figure 4.11 - Experimental and numerical force-deflection curves of SFRSCC beam specimens for distinct age at testing.

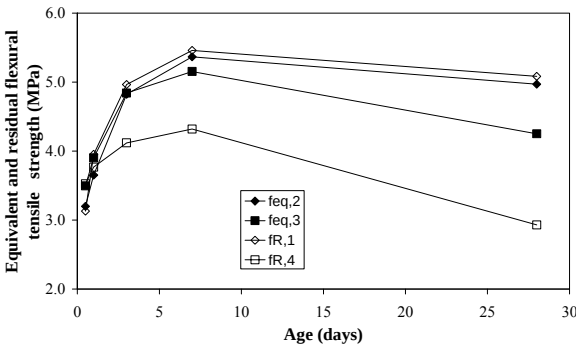

Figure 4.12 - Influence of the SFRSCC age on the equivalent and residual tensile strength parameters.

5 – STRUCTURAL BEHAVIOR

5.1 – Introduction

This chapter resumes the main achievements obtained in the research programs dedicated to the assessment of the potentialities of the developed SFRSCC for its use of structural applications (for RC slab strips failed in bending consult Barros *et al.* 2008).

5.2 – Panel prototypes

In the ambit of an applied research program, in a consortium with a precast company, SFRSCC panel prototypes were built and tested under punching and bending test setup conditions, allowing the evaluation of the SFRSCC behavior under the two most demanding load conditions for the facade panels. The panel prototypes were fabricated by the SFRSCC composition nº 1, indicated in Table 2.1. The punching tests were executed in panel prototypes of 600 × 600 mm^2 and 110 mm thick, and the flexural tests were carried out in panel prototypes of 1000 × 1000 mm^2 and the same thickness, both at an age of 7 days.

5.2.1 Panel prototypes failing in punching

As represented in Fig. 5.1a, the lightweight central region of the panel prototypes subjected to punching load is composed of a concrete layer of 30 mm thick. The procedure followed to assess the load-deflection behavior of the lightweight SFRSCC panel prototype consisted on applying a load at the centre of the panel, by means of a square steel plate of 100 mm edge and 10 mm thick. The loading sequence was executed using the vertical displacement as control variable, measured by the displacement transducer included on the loading equipment. A vertical displacement rate of 25 μm/s was prescribed, and the test procedure was stopped when punching failure was observed. The results obtained in terms of load-deflection curve are represented in Fig. 5.1b. After a short linear elastic phase, the panel entered into an elastic-cracked phase and supported an increasing load up to 40 kN. This load level was then maintained practically constant from a deflection of 1.4 mm up to a deflection of about 3 mm, representing 1% of the lightweight zone span. Then, the load suddenly fell from the 40 kN to approximately 20 kN, suggesting the occurrence of failure by punching. Fibers bridging the surfaces of the punching failure crack offered some resistance to the opening of this crack, delaying the loss of contribution of the aggregate interlock for the punching resistance. This justifies the relatively high level of residual strength that decreases very slowly with the deflection increase. The estimation of the steel fibers contribution for punching strength increase is further discussed in the section dedicated to the numerical simulation of these tests.

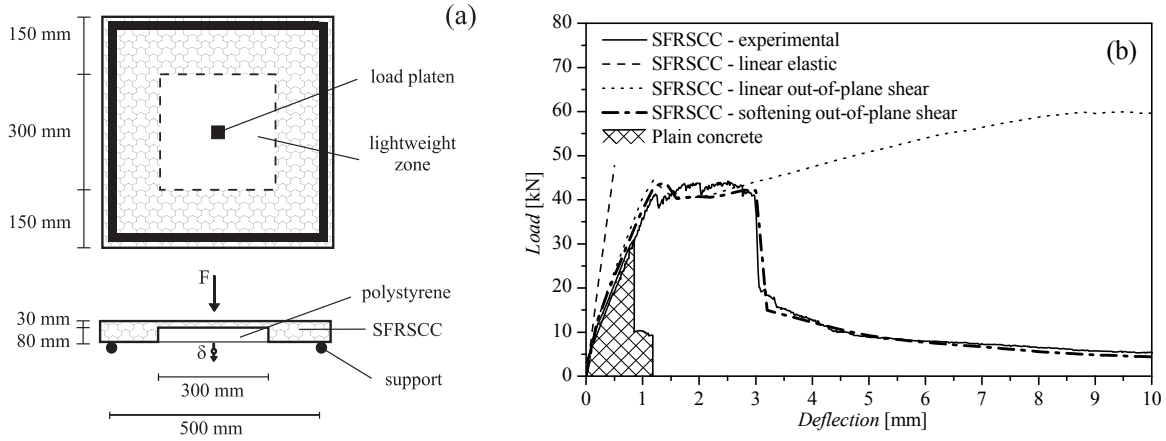

Fig. 5.1 - Punching test on panel prototype: (a) test setup, and (b) load-deflection experimental and numerical results.

5.2.2 Panel prototypes failing in bending

The panel prototypes destined for the evaluation of flexural behavior were conceived using the same lightweight concept as in punching. As represented in Fig. 5.2a, lightweight zones had also a concrete upper layer of 30 mm thick, and the thicker zones of the panel constituted a grid system of two-per-two orthogonal ribs. The panel has also a contour rib of 100 mm width. The test procedure consisted of applying a constant displacement rate (25 μm/s) at the centre of a main loading steel beam, connected to other two transversal secondary beams by means of two rollers. Load was transmitted to the four loading points at rib intersections by means of four square steel plates (100×100×20 mm^3) and four steel spheres of 20 mm diameter, in contact

with the ends of the secondary loading beams (Pereira 2006). This entire loading mechanism was idealized with the intention of assuring that, independently of the observed deflection beneath each of the four loading points, the applied load was the same in each loaded area. To obtain the vertical deflection beneath each of these four loaded areas, four displacement transducers were there installed. The supports system was constituted by eight elements placed at the ends of the grid ribs, each one was constituted by a steel plate ($100\times100\times10$ mm^3) in contact with the bottom surface of the panel, and a steel sphere of 20 mm diameter, placed between the steel plate and the ground, guaranteeing that only the vertical displacement was constrained (lifting was not prevented). The results obtained in terms of load-deflection curve are represented in Fig. 5.2b, showing that the load retaining capacity of the structure assumes relevance, in similitude to the results observed at punching tests. To simplify the analysis, only the average results will be considered. A detailed analysis can be found elsewhere (Barros *et al.* 2005). After reaching a peak load of approximately 55 kN, the panel demonstrates the ability to almost totally retain the load carrying capacity up to an average deflection of around 5 mm. Even then, the load carrying capacity decreases very slowly with the increase of the average deflection. The test sequence was stopped for a load of 15 kN (27% of the peak load) due to excess of deformation and incompatibility with the supports and the loading apparatus.

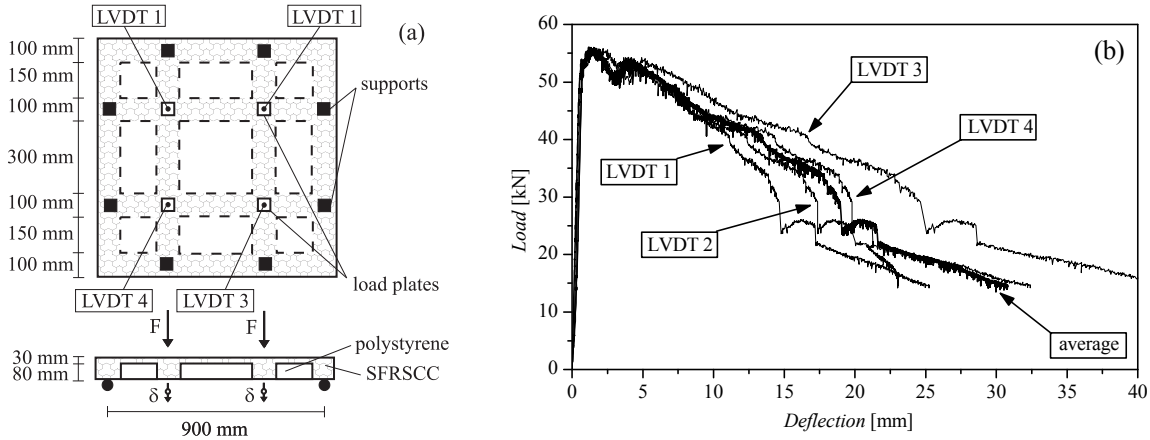

Fig. 5.2 - Flexural tests on panel prototypes: (a) test setup, and (b) typical load-deflection experimental results.

5.3 – Test with full size structural elements

With the aim of verifying if the procedures adopted in the laboratory, in the development of a SFRSCC, can be directly applicable in industrial environment, the full scale SFRSCC panel, represented in Fig. 5.3, was fabricated and tested in a precast company. The test had also the purpose of evaluating the behavior of a real panel when submitted to its dead weight and to an increase live load, up to its rupture.

Two mixtures of 400 dm^3 were made to fabricate the panel. Both concrete mixtures were stable without any indication of segregation. The spread was 600 mm and 630 mm in the mixtures 1 and 2, respectively, while the H2/H1 parameter of the L-Box test was 0.80 (the test was only carried out for the second mixture). The demolding of the panel was done in the day after it had been cast, when the SFRSCC had an age of 24 hours. The panel was demolded almost in vertical position. After that, the panel was placed in a support until the test, which occurred at 7 days of panel age. Fig. 5.4 represents the panel support conditions and the location where the deflection was measured (center of the panel). The panel was supported in four points. To simulate a uniform distributed live load, concrete plates of 500×500 mm^2, each one of 25 kg, were uniformly distributed in the area interior to the panel supports (Fig. 5.5). The panel supported 33 concrete plates, corresponding to a uniform distributed load of $8.25/(3.1\times1.5)=1.77$ kN/m^2, plus its dead weight (1.47 kN/m^2). When placing the 33rd concrete plate, an abrupt increase of deflection occurred, having the test been interrupted due to safety reasons (Fig. 5.5). When the 18th concrete plate was placed, a deflection of 24 mm was measured. When the test was interrupted, the deflection was about 44 mm and the maximum crack opening of the critical crack was around 3 mm. Fibers crossing this crack were visible. The live load of 1.77 kN/m^2 is higher than the characteristic value of the wind dynamic pressure that actuates in the major part of buildings with facade panels.

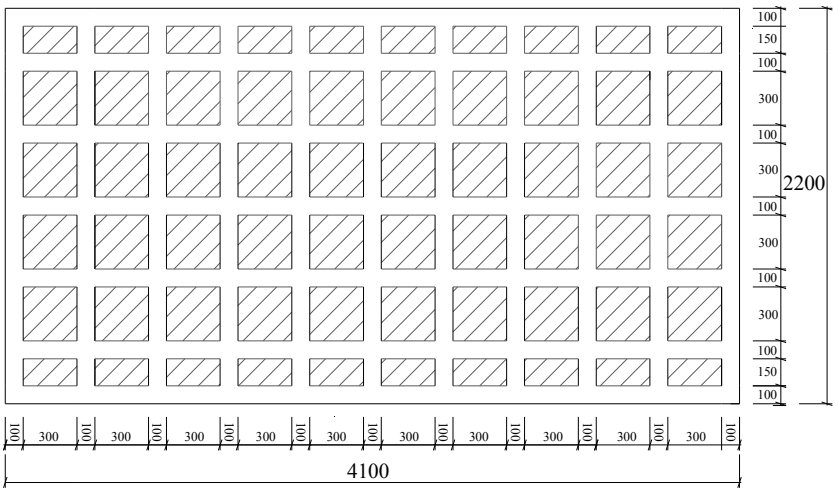

Fig. 5.3 - Panel geometry (dimensions in mm): thickness = 110mm, total vol.=0.882 m^3, Lightweight=0.36 m^3, vol. to cast=0.522 m^3, approximated weight = 1305 kg.

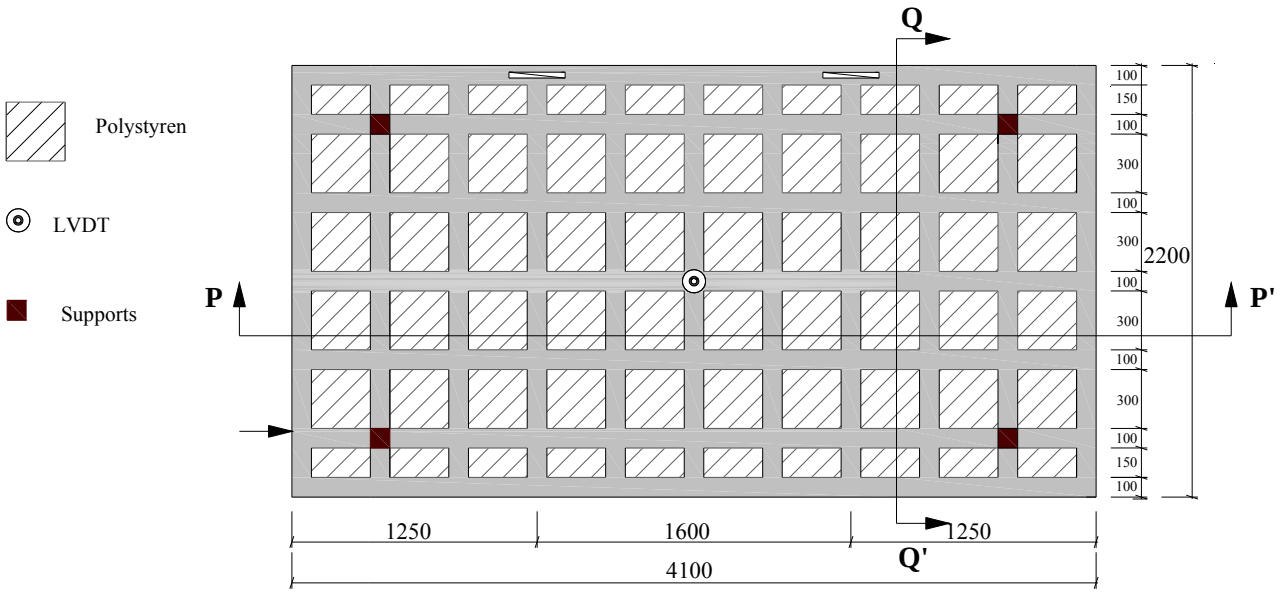

Fig. 5.4 - Setup of the loading test (dimensions in mm)

Fig. 5.5 - Final view of the panel, loaded with 33 concrete plates.

6 – FEM MODELS FOR THE ANALYSIS OF LAMINAR SFRSCC STRUCTURES

6.1 – Introduction

The structural behavior of laminar elements, the highly non-linear material behavior of hardened SFRSCC, and the determination of the fracture parameters that characterizes the SFRSCC post-peak behavior constitute the three main challenges to be resolved. In the present work, the simulation of the behavior of laminar structures was treated by employing the theory of plane shells, based on the 'Reissner-Mindlin' formulation (Barros 1995). The SFRSCC post-cracking behavior was simulated by a multi-fixed smeared crack model. Details of this smeared crack constitutive model can be found elsewhere (Gouveia *et al.* 2007). Since previous works have given indications that inverse analysis is an appropriate numerical strategy to determine the material fracture parameters (Barros *et al.* 2005), it was applied to the results obtained in the flexural tests with specimens of 7 days to determine the fracture parameters of the SFRSCC at this age (see Section 4.3.2). These numerical simulations were carried out with FEMIX 4.0 computer program, which is a software whose architecture was conceived to allow for an easy implementation of new types of finite elements and new constitutive models (Sena *et al.* 2007).

6.2 – Inverse analysis

In this work, the fracture mode I of the post-cracking behavior of SFRSCC is described by the tri-linear stress-strain softening diagram represented in Fig. 6.1b. The shape of this function is defined by a group of fracture parameters (α_i , ξ_i , G_f , f_{ct} and l_b) and the accuracy of the FEM modeling largely depends on the values of these parameters, where G_f is the mode I fracture energy (RILEM 50-FMC 1985) and l_b is the crack band width (Rots 1988). In this context, the obtained experimental results of punching and flexural tests may be predicted by a FEM model, if the correct values of the material fracture parameters are found and introduced in the constitutive model. The question is, though, what is the best strategy to obtain the accurate values for these parameters? In this work, it is suggested that the fracture parameters may be assessed by means of an inverse analysis of the flexural test results, in agreement with previous studies (Barros *et al.* 2005). The procedure consists on the evaluation of the ξ_i , α_i and G_f parameters, the ones that define the shape of the tri-linear $\sigma_n^{cr} - \varepsilon_n^{cr}$ constitutive law, leading to the minimization of the ratio between the area limited by the experimental and the numerical curves and the area underneath the experimental curve. The experimental curve corresponds to the average results observed in prismatic SFRSCC notched specimens, tested according to the RILEM TC 162-TDF recommendations, at the age of 7 days (see Section 4.3.2).

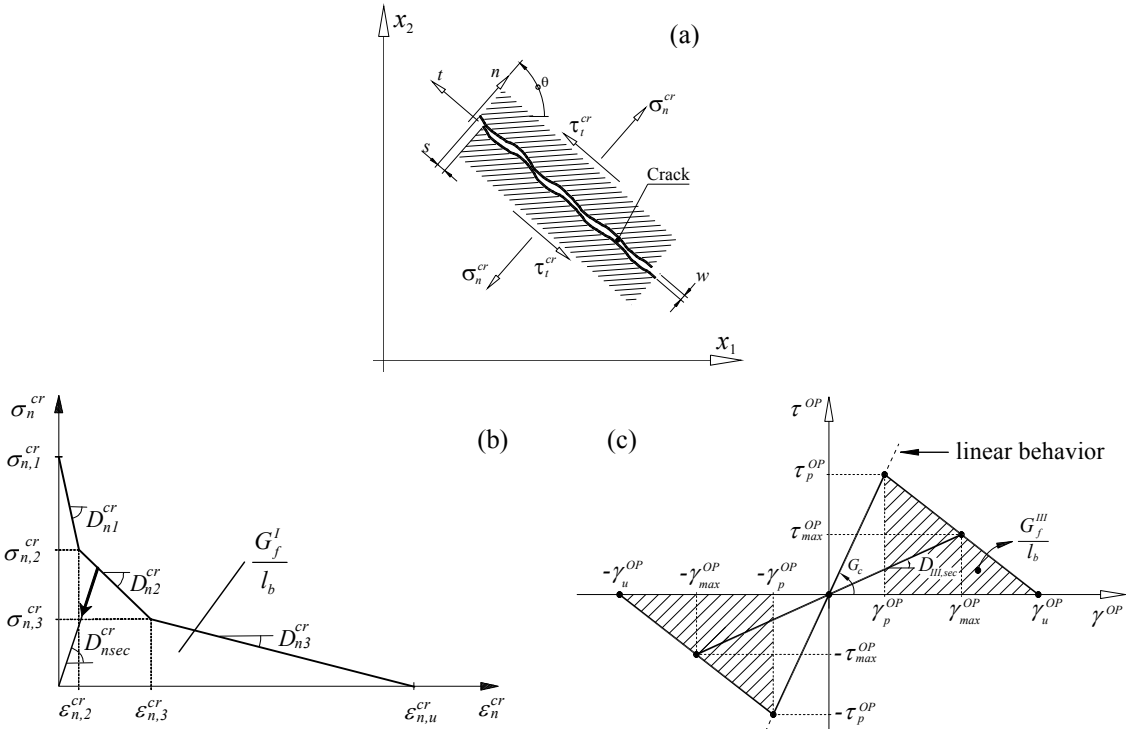

Fig. 6.1 - (a) Crack stress components, relative displacements and local coordinate system of the crack , (b) tri-linear stress-strain diagram to simulate the fracture mode I crack propagation of SFRSCC, and (c) generic out-of-plane (OP) shear stress-strain diagram to simulate fracture mode III.

The numerical curve consists of the results obtained by means of a FEM analysis (see Fig. 6.2a), where the specimen, the loading and the support conditions were simulated in agreement to the experimental flexural test setup. In this context, the specimen was discretized by a mesh of 8 node Serendipity plane stress finite elements. The Gauss-Legendre quadrature integration scheme with 2×2 integration points (*IP*) was used in all elements, with the exception of the elements at the specimen symmetry axis, where only 1×2 *IP* were used. This had the purpose of producing a trend to the development of the crack line along the specimen symmetry axis, over the aligned integration points, in agreement with the experimentally observed. Linear elastic material behavior was assigned to all elements, with the exception of the elements above the notch and along the specimen symmetry axis, where elastic-cracked behavior in tension was assumed. The crack band width, l_b, was assumed to be 5 mm, equal to the width of the notch and of the elements above. In Fig. 6.2b, the results obtained experimentally for flexural tests are compared with the ones resulting from the numerical model. A very good agreement between the experimental and the numerical curve exists. The values assumed for the fracture parameters, ξ_i, α_i and G_f, that resulted in the obtained numerical curve represented in Fig. 6.2b, are presented in Table 6.1.

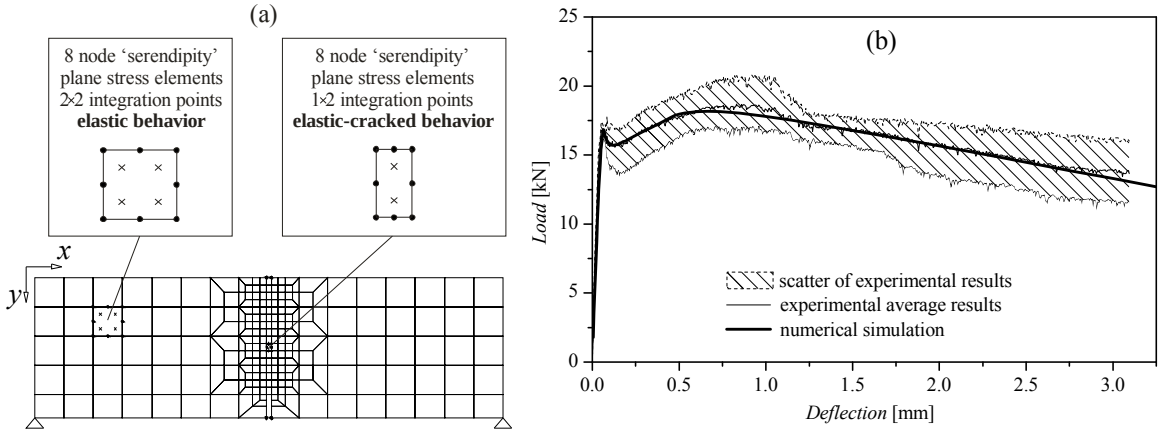

Fig. 6.2 - Three-point notched beam flexural test at 7 days: (a) FEM mesh used in the numerical simulation, and (b) obtained results.

Table 6.1. Values of the fracture parameters defining the stress-strain softening laws.

Material	$\sigma_{I,1}^{cr}$ [MPa]	$\sigma_{I,2}^{cr}$ [MPa]	$\sigma_{I,3}^{cr}$ [MPa]	$\varepsilon_{I,2}^{cr} / \varepsilon_{I,ult}^{cr}$	$\varepsilon_{I,3}^{cr} / \varepsilon_{I,ult}^{cr}$	G_f [N/mm]
SFRSCC	3.50	1.750	2.065	0.009	0.150	4.3
PC	3.50	0.525	-	0.072	-	0.08732

6.3 – Simulation of the tests with panel prototypes failing in punching

The experimental results recorded from punching tests with panel prototypes are compared with the ones obtained from the numerical simulation. For this purpose, a FEM mesh was prepared, composed of 12 per 12 eight-node Serendipity plane shell elements, each one divided in 11 layers 10 mm thick. Reminding that the panel had lightweight zones, materialized by the suppression of 80 mm of concrete at a 300×300mm^2 square central area (see Fig. 5.1a), the 8 lower layers of the finite elements at the lightweight central square zone were constituted by a fictitious material with numerically null rigidity. The remaining three upper layers, and all layers of the elements located outside the lightweight zone, were constituted by the SFRSCC, whose values for the fracture parameters are those indicated in Table 6.1, obtained from inverse analysis, as described in the previous section.

The out-of plane component of the elastic-cracked constitutive matrix was defined on the basis of a trial-and-error procedure (Gouveia *et al.* 2007). The out-of-plane shear fracture energy value that best fitted the punching failure experimental results ($G_f^{III} = 3.0\,N/mm$) was determined in this fashion, since no other laboratory test was carried out to allow its assessment by inverse analysis. The results obtained form the numerical simulation were compared with the experimental ones in Fig. 5.1b. A quite good simulation was obtained up to a deflection of 2.5 mm. For greater deflections, it is clear an over-estimation of the load carrying capacity of the panel prototype, if a linear elastic behavior is assumed for the out-of-plane shear components. At an approximate deflection of 3 mm, the load at the experimental curve suddenly falls, indicating the failure of the panel by punching, as visually found during experimental testing. This load decay, not possible to be simulated by assuming linear elastic behavior for the out-of-plane shear components

was, however, well captured by the numerical simulation when the bilinear function represented in Fig. 6.1c was used to model the softening behavior of out-of-plane shear components, with $G_f^{III} = 3.0\,N/mm$ and assuming a crack band width l_b equal to the square root of the area of the corresponding integration point. The abrupt load decay from approximately 42 kN to 25 kN, observed experimentally, was almost perfectly followed by the numerical model, as well as the observed subsequent stage of smooth load decay.

The strategy proposed here to estimate the contribution of steel fibers for punching behavior is based on the establishment of a softening stress-strain law diagram for plain concrete (PC) in tension. The remaining characteristics of the numerical simulation were the same ones as used for the previous SFRSCC material nonlinear analysis. The softening stress-strain law for PC in tension was established in accordance with (CEB-FIP 1993) recommendations. Assuming that the tensile strength is the same for SFRSCC and for the equivalent PC, the fracture parameters defining a bilinear stress-strain diagram ($D_{n2}^{cr} = D_{n3}^{cr}$ in Fig. 6.1b) were determined, and are indicated in Table 6.1. Fig. 5.1b represents the predicted deformational behavior of a PC panel prototype, from which it can be observed that PC has a punching strength that is around 70% of the punching strength of SFRSCC, and the energy absorbed up to the failure of plain concrete panel represents only around 15% of the energy absorbed by SFRSCC panel.

7 – CONCLUSIONS

The present work resumes the main achievements found in research projects carried out at the University of Minho, in consortium with Companies interested in the technology of steel fiber reinforced self-compacting concrete (SFRSCC). These projects dealt with:
1) Development of cost competitive SFRSCC of enough post-cracking residual strength in order to allow its use on some structural applications. It was verified that, using local materials and a content of cement lower than 400 kg/m^3 (apart the steel fibers, cement was the most expensive material in the composition) it is possible to develop a SFRSCC of an average compressive strength and an equivalent flexural tensile strength higher than 50 MPa and 5 MPa, respectively, at 7 days;
2) Characterization of the material properties, mainly in compression and flexural, not only in static but also in cyclic loadings. Special focus was given to the influence of the SFRSCC age on the compression stress-strain relationship, Young's modulus, compressive strength, and flexural tensile strength parameters;
3) Based on the experimental results, the equations proposed by CEB-FIP Model Code 1993 were adjusted to simulate the SFRSCC compression behavior from 12 hours to 28 days;
4) A model was proposed to simulate the SFRSCC cyclic compression behavior;
5) A lightweight SFRSCC panel system, for building façades, was developed and its flexural and punching resistance was assessed carrying out flexural tests able to promote these types of failure modes. The obtained results revealed the great contribution that fiber reinforcement has provided;
6) Full scale SFRSCC panels were produced and tested in a precast company in order to establish the best practices of technology transfer from laboratory to factory;
7) The constitutive law that defines the SFRSCC fracture mode I can be obtained from inverse analysis, using the results recorded in the flexural tests for this purpose;
8) FEM based on the nonlinear fracture mechanics can be used to predict, with high accuracy, the behaviour of laminar SFRSCC structures up to their collapse. Mindlin-Reissner shell theory can be used to simulate complex failure modes, like punching, if a softening constitutive law is used to model the out-of-plane shear components.

8 – ACKNOWLEDGEMENTS

The study reported in this paper is part of the research program *PABERPRO – Conception and implementation of production system of lightweight steel fibre reinforced self-compacting concrete panels"* supported by Program POCI 2010 – IDEIA, Project nº 13-05-04-FDR-00007, contract reference ADI/2007/V4.1/0049. This project involves the Companies PREGAIA and CIVITEST, and the University of Minho. The author wish to acknowledge the materials generously supplied by Bekaert (fibres), SECIL (cement), Degussa (superplasticizer), and Comital (limestone filler). Special acknowledgement is given to the researchers that collaborated in the projects within the ambit of the present topic.

9 – REFERENCES

Banthia, N.; Trottier, J., "Concrete reinforced with deformed steel fibres, Part I: Bond slip mechanisms", ACI Materials Journal, 91(5): 435–446, 1994.

Barros, J.A.O.; Santos, S.P.F.; Lourenço, L.A.P., "Flexural behaviour of steel fibre reinforced self-compacting concrete laminar structures", HAC2008, 1st Spanish Congress on Self-Compacting Concrete, Valencia, Spain, 18-19 February 2008.

Barros, J.A.O.; Cunha, V.M.C.F.; Ribeiro, A.F.; Antunes, J.A.B., "Post-Cracking Behaviour of Steel Fibre Reinforced Concrete", RILEM Materials and Structures Journal, 38(275), 47-56, 2005.

Barros, J.A.O. ; Pereira, E.B.; Cunha, V.M.C.F.; Ribeiro, A.F.; Santos, S.P.F.; Queirós, P.A.A.A.V. (2005). "PABERFIA- Lightweight sandwich panels in steel fiber reinforced self compacting concrete." *Technical Report 05-DEC/E-29*, Dep. Civil Eng., School Eng. University of Minho, 63 pp., 2005.

Barros, J.A.O., "Behaviour of fibre reinforced concrete – experimental analysis and numerical simulation", PhD Thesis, Dep. Civil Eng., Faculty of Eng. of Oporto University, 502 p, December 1995. (in Portuguese)

Cunha, V.M.C.F.; Barros, J.A.O.; Sena-Cruz, J.M., "Pullout behaviour of hooked-end steel fibers in self-compacting concrete", Technical report 07-DEC/E-06, Dep. Civil Eng., School Eng. University of Minho, 90 p., April 2007a.

Cunha, V.M.C.F.; Barros, J.A.O.; Sena-Cruz, J.M., "Modelling the influence of age of steel fibre reinforced self – compacting concrete on its compressive behaviour", in press, RILEM Materials and Structures Journal, 2007b.

Cunha, V.M.C.F.; Barros, J.A.O.; Sena-Cruz, J.M, "Compression behaviour of steel fibre reinforced concrete (age influence and modelling)", Technical report no. 06-DEC/E-04, Department of Civil Engineering, University of Minho, 49 pp., 2006.

EFNARC, "Specification and Guidelines for Self-Compacting Concrete", ISBN 0 9539733 4 4, 32 pp., 2002.

EN197-1:2000, "Cement. Composition, specifications and conformity criteria for low heat common cements", ISBN: 058036456 9, 52 pp, 2000.

Gomes, P.C.C., "Optimization and characterisation of high-strength self-compacting concrete", PhD Thesis, Universitat Plitècnica de Catalunya, Escola Técnica Superior D'Enginyers de Camins, Canals i Ports de Barcelona, 2002.

Gonçalves, D.M.F.; Barros, J.A.O., "Cyclic compression behaviour of steel fibre reinforced self-compacting concrete – experimental and analytical research", Technical report CT_I&D/1107, November 2007. (in Portuguese)

Gouveia, A.V.; Barros, J.A.O.; Azevedo, A.F.M.; Sena-Cruz, J.M., "Crack Constitutive Model to Simulate the Behavior of Fiber Reinforced Concrete Structures Failing in Punching", CMNE 2007 - Congress on Numerical Methods in Engineering and XXVIII CILAMCE - Iberian Latin American Congress on Computational Methods in Engineering, Abstract pp. 287, Paper nº 232 published in CD – FEUP, 13 pp., Porto, 13-15 June 2007.

Groth P., "Fibre reinforced concrete - Fracture mechanics methods applied on self-compacting concrete and energetically modified binders", PhD Thesis, Department of Civil and Mining Engineering, Lulea University of Technology, Sweden, 2000.

Li, V.C.; Chan, Y.-W., "Determination of interfacial debond mode for fibre-reinforced cementitious composites", ASCE Journal of Engineering Mechanics, 120(4): 707–719, 1994.

MC90, "CEB-FIP Model Code 1990: Design code", Thomas Telford, Lausanne, 1993.

Naaman, A.E.; Najm, H., "Bond-slip mechanisms of steel fibres in concrete", ACI Materials Journal, 88(2): 135–145, 1991.

Okamura, H.; Maekawa, K., "Nonlinear analysis and constitutive models of reinforced concrete", Gihodo-Shuppan Press, Tokyo, Japan, 1991.

Pereira, E.N.B., "Steel Fibre Reinforced Self-compacting Concrete: from material to mechanical behaviour", dissertation for Pedagogical and Scientific Aptitude Proofs, Department Civil Engineering, University of Minho, 188 pp, 2006. <http://www.civil.uminho.pt/composites>

RILEM 50-FMC, "Determination of the fracture energy of mortar and concrete by means of three-point bending tests on notched beams", Materials and Structures, Vol. 85, Nº 85, pp. 285-290, 1985.

Rots, J.G., "Computational modeling of concrete fracture", Dissertation, Delft University of Technology, 1988.

Sena-Cruz, J.M.; Barros, J.A.O.; Azevedo, A.F.M.; Gouveia, A.V., "Numerical Simulation of the Nonlinear Behaviour of RC Beams Strengthened with NSM CFRP Laminate Strips", CMNE 2007 - Congress on Numerical Methods in Engineering and XXVIII CILAMCE - Iberian Latin American Congress on Computational Methods in Engineering, Abstract pp. 289, Paper nº 485 published in CD – FEUP, 20 pp., Porto, 13-15 June 2007.

Vandewalle, L. et al., "Test and design methods for steel fiber reinforced concrete. Recommendations for bending test", RILEM Materials and Structures Journal, 33 (225), 3-5, 2000.

Vandewalle, L. et al., "Test and design methods for steel fibre reinforced concrete - Final Recommendation", Materials and Structures 35 (253), 579-582, 2002.

Wang, C.Z.; Guo, Z.H.; Zhang X.Q., "Experimental investigation of the complete stress-strain curves of concrete under cyclic loading", US/PRC Workshop on Seismic Analysis and Design of Reinforced Structures, Ann Arbor, Michigan, USA, 1981.